Graphical Abstract

In-field railhead crack detection using digital image correlation

Knut Andreas Meyer,Daniel Gren,Johan Ahlström,Anders Ekberg

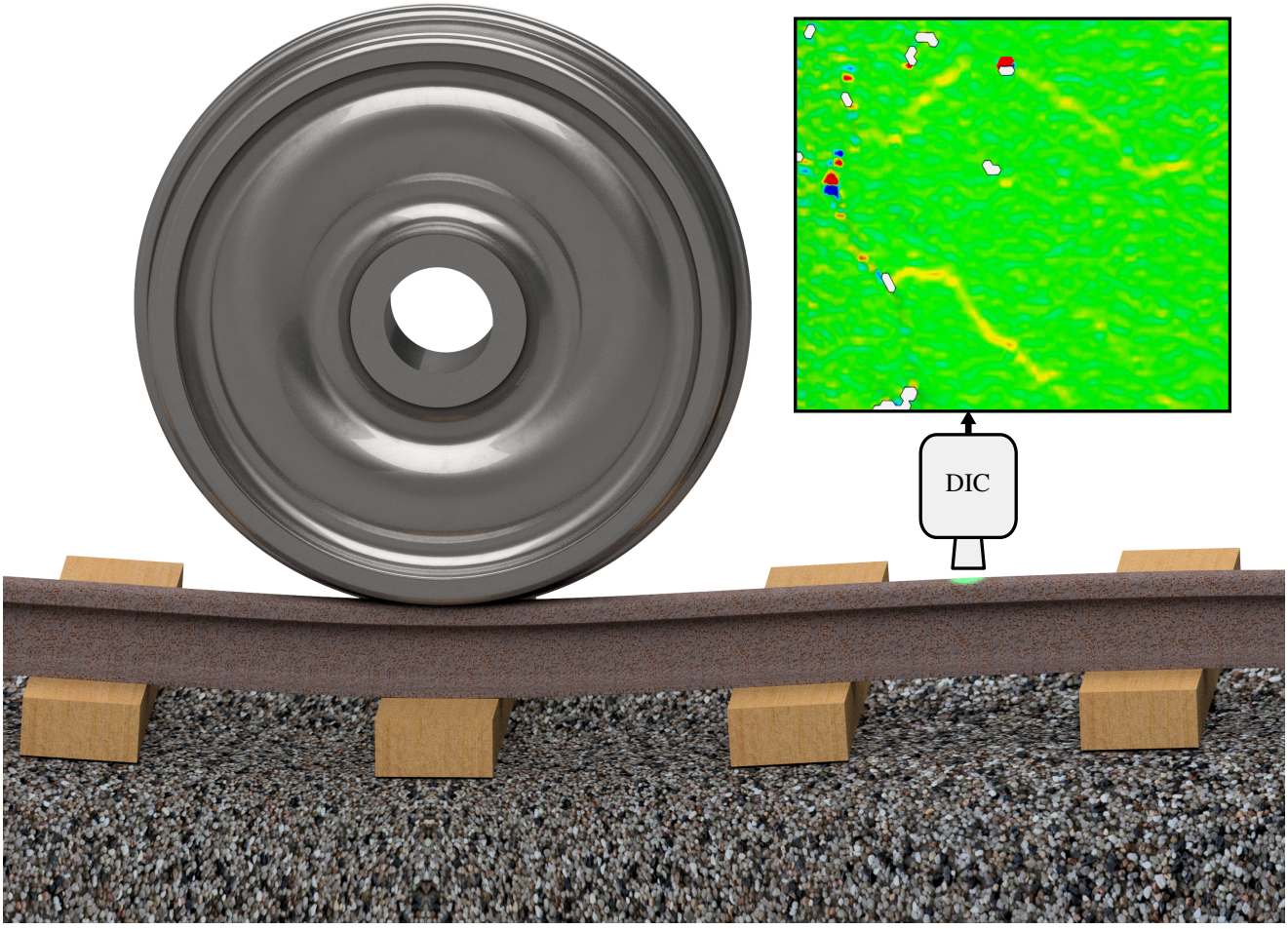

Highlights

In-field railhead crack detection using digital image correlation

Knut Andreas Meyer,Daniel Gren,Johan Ahlström,Anders Ekberg

- A novel application of DIC for railhead crack detection is proposed.
- Field samples are studied under realistic loading conditions.
- The intricate 3D crack network is characterized.

In-field railhead crack detection using digital image correlation

Knut Andreas Meyer[a,*], Daniel Gren[b], Johan Ahlström[b] and Anders Ekberg[c]

[a]Division of Material and Computational Mechanics, Department of Industrial and Materials Science, Chalmers University of Technology, SE-41296, Gothenburg, Sweden

[b]Division of Engineering Materials, Department of Industrial and Materials Science, Chalmers University of Technology, SE-41296, Gothenburg, Sweden

[c]Division of Dynamics, Department of Mechanics and Maritime Sciences, Chalmers University of Technology, SE-41296, Gothenburg, Sweden

ARTICLE INFO

Keywords:
Conditioning monitoring
Digital image correlation
Crack detection
Railway maintenance
Safety

Abstract

A significant challenge for railway infrastructure managers is to know when and how to maintain rails. Often, the critical missing information is the current health status, in particular information about rail cracks. Therefore, a new method for rail crack detection is proposed. By utilizing a train-mounted camera system, a single measurement train can monitor a large rail network. The system uses Digital Image Correlation (DIC) to measure the strain fields due to rail bending caused by the measurement train. Promising results are obtained under laboratory conditions. The identified cracks are correlated to the actual crack network, characterized by serial-sectioning microscopy. Furthermore, finite element simulations show the method's high sensitivity to crack depths. Knowing the crack depths enable infrastructure managers to optimize the rail maintenance.

1. Introduction

In 2012, the annual cost for railway infrastructure maintenance and renewal across Europe was estimated to be between 15 and 25 billion Euros[7]. The cost of rail defects alone in the 1990s was estimated at 2 billion Euros a year[3]. This figure equates to about 6700€, on average, per kilometer in Europe's 300 000 km long railway network[13]. These costs do not include the socio-economic costs associated with delays due to unscheduled repairs. Today, many infrastructure managers do not have sufficiently accurate descriptions of the damage state in the rails. To mitigate this lack of information, they need efficient and reliable condition monitoring systems. Manual visual inspection is still commonly used, but it requires highly trained personnel and is labor intensive. Several methods for automated condition monitoring already exist, with the most common Non-Destructive Testing (NDT) methods being ultrasonic and eddy-current[22].

Ultrasonic testing can detect relatively large cracks at high inspection speeds. Speeds up to 100 km/h have been reported[8], noting that the accuracy decreases as the operating speed increases. As for the detectable defect size, Marais and Mistry[14] were able to find cracks with a linear size down to 5 mm. Hence, ultrasonic testing is mostly applicable to find deep cracks. However, these might be concealed by surface cracks[3].

Eddy-current testing complements the ultrasonic testing as it can detect surface defects. Rajamäki et al.[20] found a penetration depth of 3 mm to be the practical limit. However, the resolution decays exponentially with depth. On the other hand, at ideal laboratory conditions, cracks located deeper have been identified, see e.g. Kishore et al.[10] who found cracks at a 5 mm depth. Similar to ultrasonic testing, high inspection speeds (up to 70 km/h) have been reported in the literature[19].

In addition to the two most common methods described above, several others have been investigated in the literature. A method based on magnetic flux leakage could identify artificial surface cracks but was less accurate for natural cracks[5]. The "alternating current field" method detects disturbances of induced current in a thin layer close to the surface, caused by surface defects. The method is less sensitive to the sensor-

*Corresponding author
knut.andreas.meyer@chalmers.se (K.A. Meyer); daniel.gren@chalmers.se (D. Gren); johan.ahlstrom@chalmers.se (J. Ahlström); anders.ekberg@chalmers.se (A. Ekberg)
ORCID(s): 0000-0001-7280-4436 (K.A. Meyer); 0000-0002-5128-8951 (D. Gren); 0000-0002-2672-4547 (J. Ahlström); 0000-0002-3219-1855 (A. Ekberg)

rail spacing compared to ultrasonic and eddy-current testing. Furthermore, quite accurate crack sizes and inclinations can be measured[22]. However, the inspection speed is low (2-3 km/h)[8]. Another approach is to use the thermoelastic effect that causes a temperature change due to an applied load. Greene et al.[6] showed that by using differential imaging, the surface defects become visible. As an alternative to applying a mechanical load, other heating sources, such as eddy-current, have also been used[1].

While the various automated approaches discussed above have many advantages, visual inspection by experienced staff is still a common approach. Inspired by this, researchers have investigated the use of surface image processing to detect surface rail defects [4, 25, 27, 11]. However, this approach has significant challenges in uncontrolled environments due to, e.g., contaminants on the rail surface.

Digital Image Correlation (DIC) is often employed in mechanical testing to calculate the strain fields. With this method, a crack is detected by the strain concentration due to it opening and thus before it can be observed on the unloaded surface[9]. DIC can also be used to find cracks in concrete structures, see Mohan and Poobal[17] for an overview. DIC uses differences between two images to detect cracks. Jessop et al.[9] used the difference between the undamaged and the damaged states. In this paper, however, we consider the difference between two images at different load levels. A passing train subjects the rail to a varying bending moment. The proposed system is mounted on the train and consists of cameras at two positions. Hence, the system allows automatic crack characterization along a railway line. The method is less sensitive to surface contaminants than direct optical methods, as the displacements are evaluated as opposed to the structure. In fact, surface contaminants may even improve the contrast and hence the resolution.

The purpose of this study is to investigate the feasibility of this novel rail crack detection method. First, the methodology for rail crack detection using DIC is described, followed by the analysis and experimental setup used to verify the methodology's feasibility. Section 4 contains the results of this verification using a field rail sample. Additionally, Section 5 includes finite element simulations that show how the surface strains measured with DIC are affected by different crack morphologies. Finally, Section 6 discusses the present findings, the remaining challenges, and potential future extensions of the proposed method.

2. Description of the proposed method

Rails, sleepers and the ground deflects as the train rolls over, as illustrated in Figure 1. These results are calculated for a freight train with a 25-ton axle load using the methodology described later, see Section 5.1. The rail deflections give rise to bending moments in the rail. Figure 1 shows that the bending moment in the middle of each wagon is approximately zero. Camera A can then take a reference image, showing the rail surface without an applied bending moment. When the train has moved so that Camera B is in Camera A's previous position, Camera B acquires an image of the same area as Camera A's reference image. This new image shows the surface being affected by tensile strains due to a positive rail bending moment. These tensile strains cause the cracks to open, see Figure 2. The crack opening cause a displacement jump over the crack mouth leading to an infinite strain. However, in DIC, the strain is calculated based on displacement between points with a finite spacing. Therefore, the strain illustrated in Figure 2 is not a Dirac delta function. If the point spacing is small enough, a high strain concentration is detected around the crack mouth. This strain concentration is the proposed crack indicator.

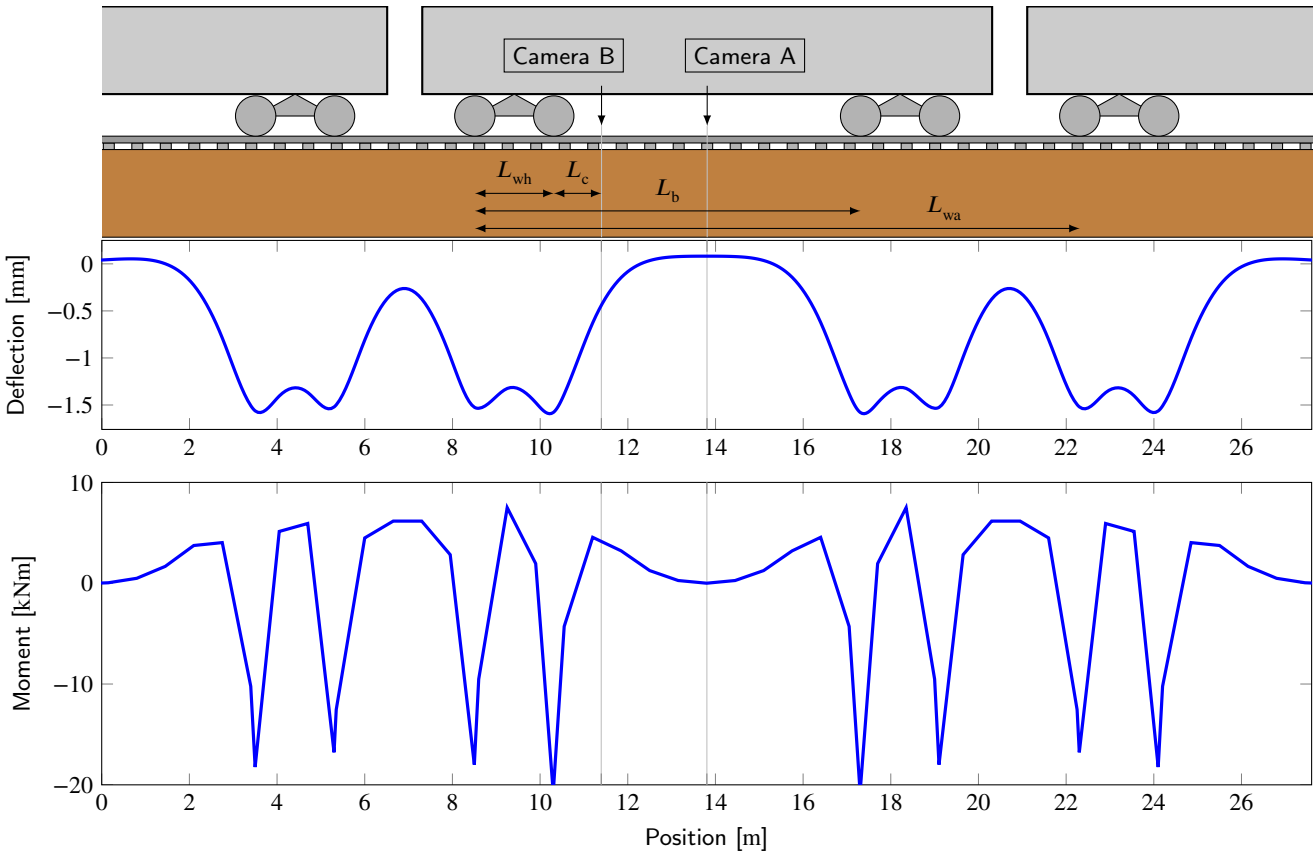

Figure 1: Rail deflection and bending moment due to a train passage. Camera A measures the undeformed rail surface while Camera B measures the deformed surface.

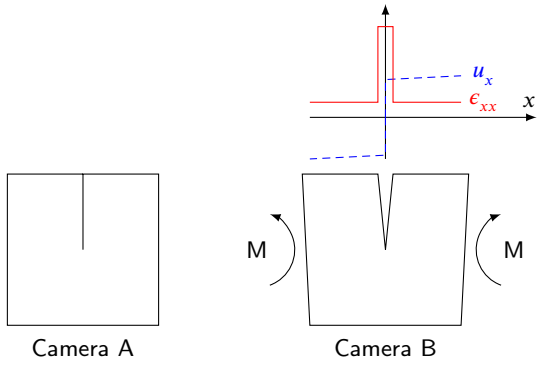

Figure 2: Illustration of the measured strain around a crack mouth in a rail subjected to a positive bending moment

3. Experimental setup

The initial evaluation of the crack detection method consists of two experimental parts. First, a rail sample is mounted in a test rig, subjected to a bending moment, and analyzed using DIC. Second, the crack networks in the examined rail part are characterized by serial sectioning. The investigated field sample was taken from the Swedish mainline (Gothenburg-Stockholm) and has sustained 11 years of traffic, corresponding to approximately 165 MGT. Further details, including its chemical composition, are given in Meyer et al. [16].

3.1. Crack detection using DIC

Two rail field samples were connected by threaded rods, as shown in Figure 3. Two hydraulically connected cylinders load the samples in 4-point bending. This setup gives a constant bending moment in the part of the rail located between the cylinders. The hydraulic pressure was controlled by a manual pump and measured by an electronic pressure sensor.

The commercial GOM system relies on a speckle pattern to create a 3-dimensional surface. We applied this pattern by first painting the railhead black, followed by adding a white speckle. The objective lens tailored for the smallest available

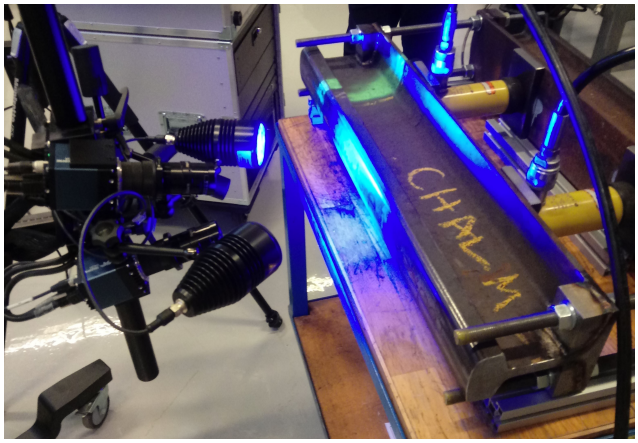

(a) Picture of DIC experiment

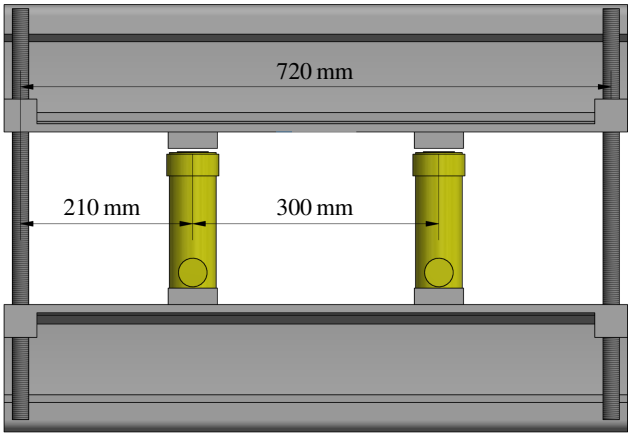

(b) Schematic of bending fixture

Figure 3: DIC experimental setup with the yellow hydraulic cylinders exerting a 4-point bending in the rail samples.

fields of view was chosen to improve the resolution. Stitching together eight different camera positions (2x4) increased the covered portion of the rail. The strains were measured for the unloaded reference state and two additional pressure levels, corresponding to bending moments of approximately 7.5 kNm and 15 kNm.

Figure 4 shows that strain concentrations can be observed at 7.5 kNm bending moment. However, the Signal to Noise Ratio (SNR) is rather low. This ratio is improved for 15 kNm, in Figure 4b, and the strain concentrations appear much clearer. The results in Figure 1 only show a 3.8 kNm bending moment. However, this moment can be increased to above 10 kNm following the optimization of train parameters in Section 5.1.

3.2. Rail sectioning

The proposed crack detection method is based on surface strains. To investigate how this method performs, detailed information about the true crack network is required. To this end, the analyzed section of the rail was extracted and characterized using serial sectioning and microscopy, see Figure 5. The extracted sample was surface ground, followed by polishing, in increments of approximately 0.25 mm. From the initial height, h_0 in Figure 5b, 9 mm was taken off starting from the gauge corner. A 1 mm wide, 0.25 mm deep, reference line for positioning was milled on one side. This line is shown in Figure 5b.

Using a 5X objective lens, resulting in a pixel size of 0.88 µm, 74 mm along the rail was characterized. Multiple image tiles were taken and merged into one image. For this merging to work efficiently, a perfectly polished surface is not favorable. For that reason, and from a time-efficiency perspective, grinding marks are still clearly visible in Figure 6. A semi-automated procedure for generating binary images was therefore adopted. Two image layers were created, where the bottom layer contained the raw image. Large dark areas in the bottom layer were filled to become fully black. In the initially transparent top layer, a stylus was used to mark cracks by a 10 pixel (8.8 µm) wide line. After that, we binarized the bottom layer with a threshold of 3. The initial image had 255 grayscale levels, where 0 was black. Hence, only very dark areas became black. Subsequently, Gaussian filtering (size 20.5 pixels), followed by a binarization (threshold 127), was applied three times to smoothen the image. At this point, the binarized bottom layer contained all large defects that could be identified automatically. As a final step, the top layer, with cracks marked by stylus, was projected onto the bottom layer.

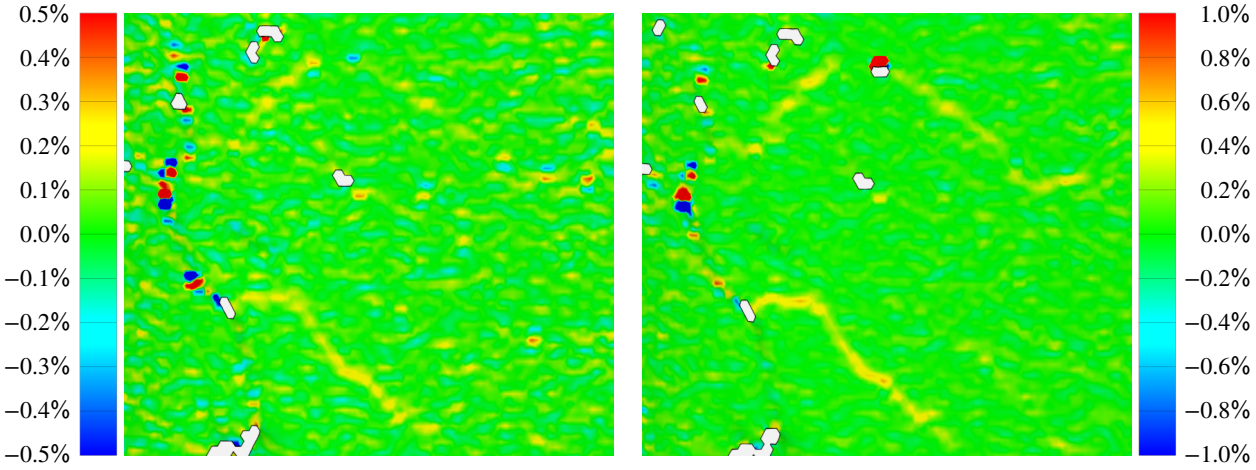

(a) $M = 7.5\,\mathrm{kNm}$ (b) $M = 15\,\mathrm{kNm}$

Figure 4: Surface strain distribution along the rail (horizontal in this figure), measured by DIC.

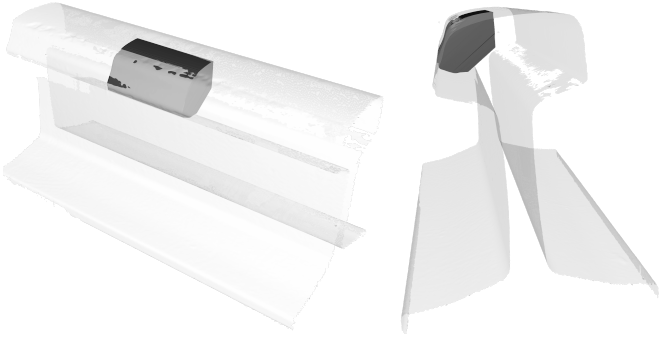

(a) Sample's location in a 3d-scanned model of the rail.

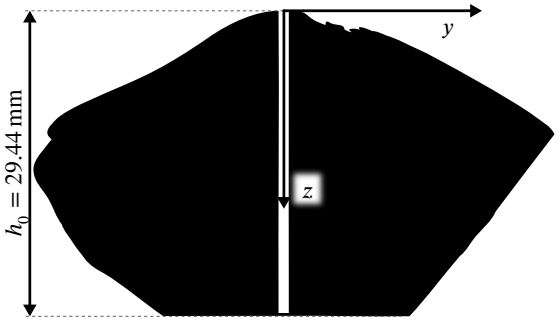

(b) Sample profile including reference mark (white line). The gauge corner is on the left side.

Figure 5: The extracted sample used to characterize the crack networks

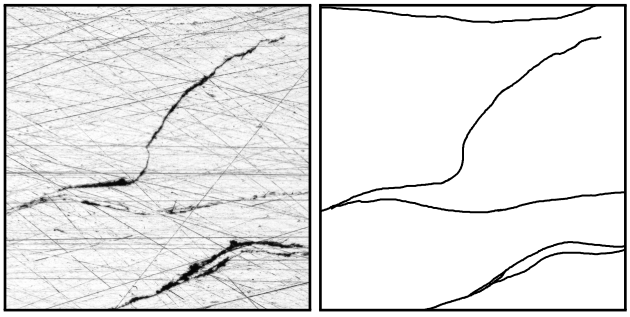

(a) Original grayscale optical microscopy image (b) Processed, binary, image

Figure 6: Example of conversion from optical microscopy images to binary images. The shown images are $1.5\,\mathrm{mm} \times 1.5\,\mathrm{mm}$.

4. Experimental results

4.1. DIC measurements

As described in Section 3.1, a bending moment of 15 kNm was chosen to display clear results. The strain field in Figure 7 is visualized for that bending moment. The reference mark, see Figure 5, is on the right side of the strain field. The reference line in Figure 7 also shows the horizontal direction in the section images that is along the rail. Hence, it is perpendicular to the reference mark shown in Figure 5b.

Two types of artifacts are observed in Figure 7. First, the white areas are places where the stereo camera vision could not identify the surface. One reason can be that it was not possible to create a surface based on the reference image. The other reason would be that the algorithm could not find a correlation to the corresponding pattern in the reference image. In either case, however, the white artifacts correspond well with severe surface irregularities. The artifacts typically occur at the crack mouths, as can be observed at reference

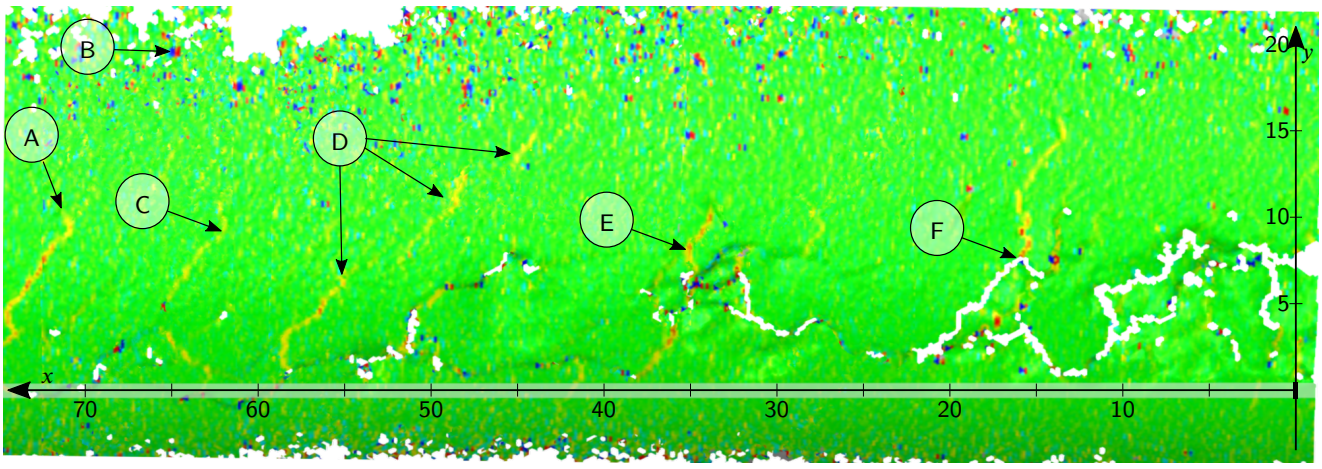

Figure 7: DIC results viewed from above the microscopy sections. The black rectangle shows the location of the reference mark, and axes correspond to the axes in Figure 8 with dimensions in mm. The same strain scale as in Figure 4b is used.

mark "F" in Figure 7. Here, the artifact is located in the lower part of the crack mouth, where the geometry is too irregular to be accurately captured by the DIC system. In the upper part, the strain concentration is visible.

The second artifact is the red and blue dots. They typically occur in pairs (see e.g. reference mark "B"). This result implies that high strains of opposite signs are detected close to each other, and the effect cancels out. As these appear just at points and do not coalescence into bands, they can be identified as non-physical artifacts. Two images were taken at each load level when acquiring the DIC results. When comparing these, the red and blue pairs do not remain constant, as opposed to the images' remaining features. Hence, we conclude that these pairs are just random errors stemming from the DIC image processing.

The DIC results provide two relevant sources of information. Firstly, an accurate 3D-map of the rail surface is obtained. This map describes the surface state and the degree of spalling. Secondly, and the primary purpose of the present study, is the strain field due to rail bending. As previously discussed, some strain concentrations continue from regions with high irregularity (e.g. at "F" and "E"). For the bands denoted by "D", several bands almost coalesce into one very long band. At "A" and "C" there are also pronounced bands of high strain concentration. All of these results were the type of patterns that was expected based on the simple illustration in Figure 2.

4.2. Rail sectioning

While the spacing between each microscopy section was 0.25 mm, due to space constraints, Figure 8 only includes a few sections. On the right side, the side view of the sectioned part's profile is shown for clarity. Ground off material is marked with a gray color. The vertical arrow indicates the approximate maximum width of the sample's surface. The sections in Figure 8 were processed further to improve crack visibility and reduce the manuscript's file size[1]. The full-sized images are available as supplemental material, see `MicroscopySections.zip`. These binary images are from the 14 first sections (down to $z = 3.25$ mm). Thereafter, the amount of new information was limited, and only the sections at 5.0 mm, 7.0 mm, 9.0 mm were binarized.

The first section, seen in Figure 8a, was made after a skim pass in the surface grinder. Several cracks are transverse to

[1] First, the resolution was decreased by scaling the image down with 80%. Second, it was filtered by a Gaussian filter with size 1 before a threshold of 2 (grayscale 0-255, where 255 is white) was applied. Finally, the resolution was again reduced by 50%.

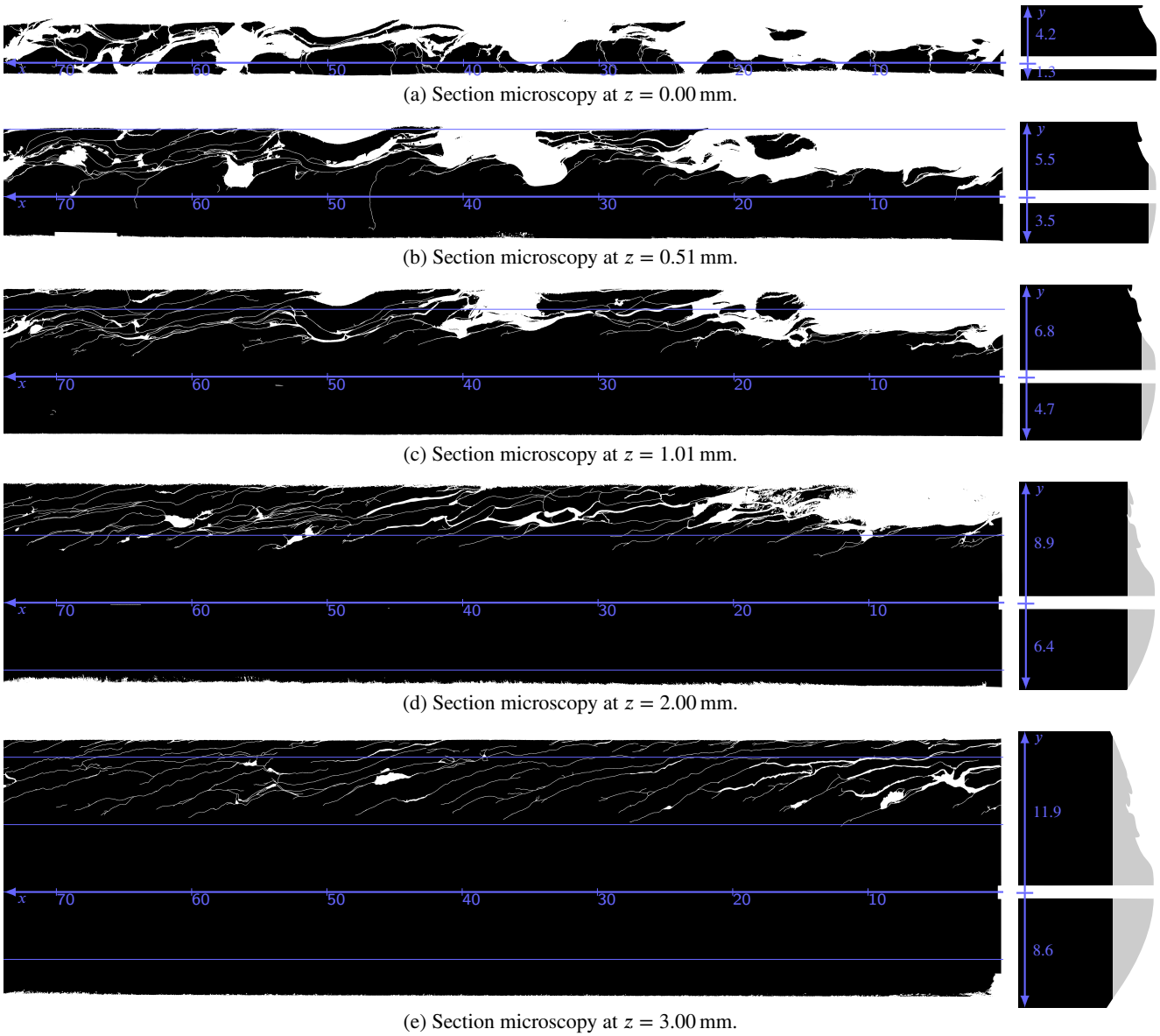

(a) Section microscopy at $z = 0.00\,\text{mm}$.

(b) Section microscopy at $z = 0.51\,\text{mm}$.

(c) Section microscopy at $z = 1.01\,\text{mm}$.

(d) Section microscopy at $z = 2.00\,\text{mm}$.

(e) Section microscopy at $z = 3.00\,\text{mm}$.

Figure 8: Sections showing the crack patterns with inverted colors compared to Figure 6. All coordinates are in mm, the horizontal lines have 5 mm spacing, the numbers next to the positive and negative y-axes denote the respective axis' length and the z-coordinate is defined in Figure 5b.

the section, as expected from the DIC results. However, only three of these remain transverse in the following two images, see $x = 4\,\text{mm}$, $x = 47\,\text{mm}$, and $x = 65\,\text{mm}$ in Figure 8b. There are no such cracks in the section at $z = 1.0\,\text{mm}$ in Figure 8c. The severe surface irregularities are observable in the first 2 mm of depth. At $z = 3\,\text{mm}$, Figure 8e, there are still rather large voids. Some seem to be subsurface defects, while others, such as in the upper right corner, seem to be surface defects (cf. Figure 8d). From Figure 8f ($z = 5\,\text{mm}$), however, only thin cracks exist and the amount of cracks is also decreasing. At $z = 9\,\text{mm}$ (Figure 8h), only a few cracks very close to the surface remain. In summary, the maximum crack depth (measured normal to the surface) in the investigated rail is approximately 3 mm.

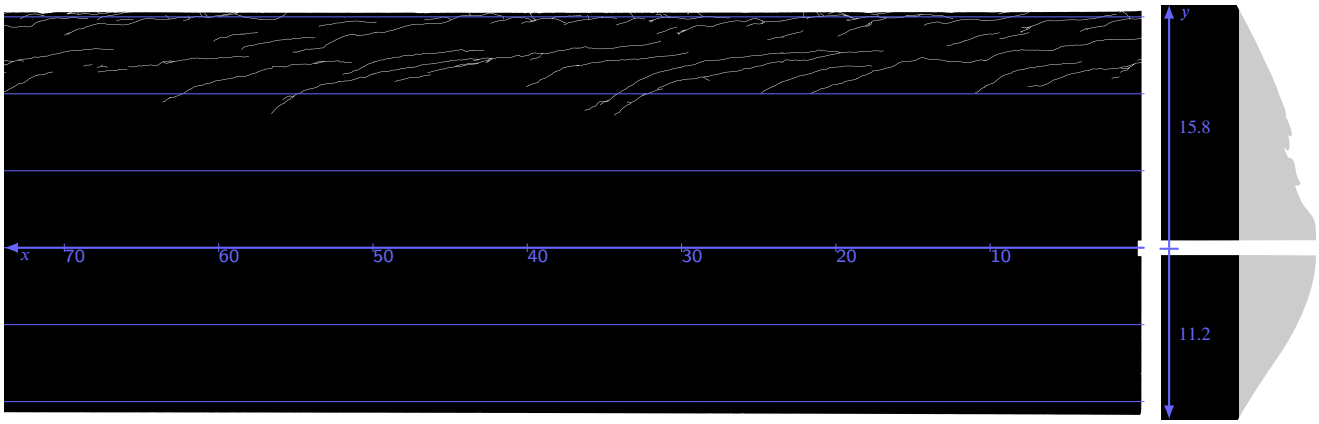

(f) Section microscopy at $z = 5.00\,\text{mm}$.

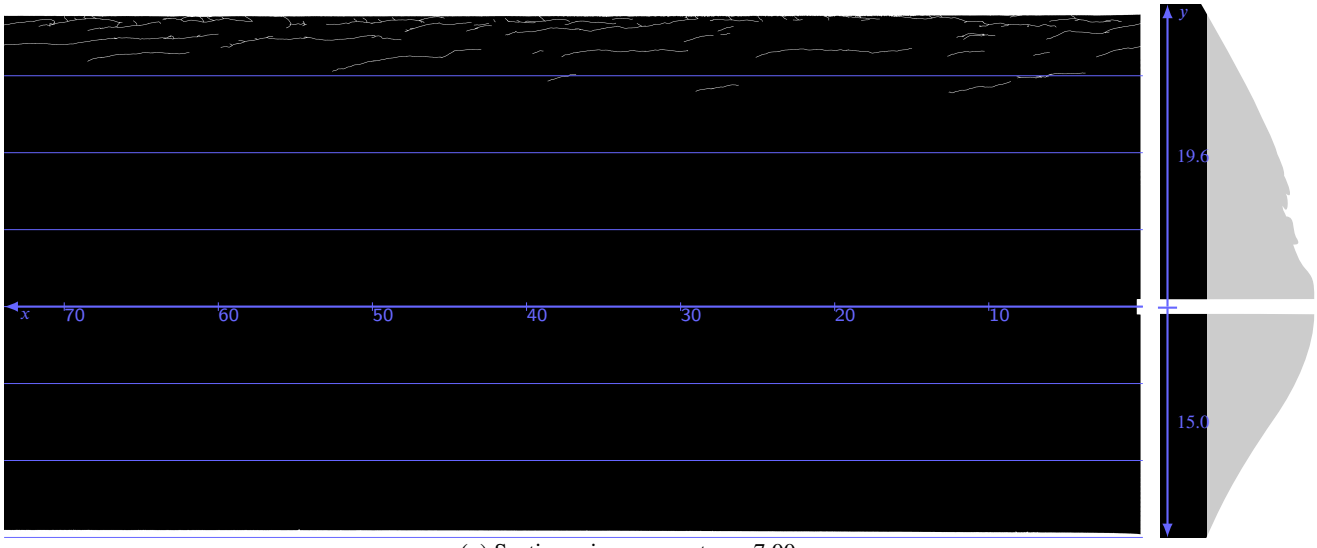

(g) Section microscopy at $z = 7.00\,\text{mm}$.

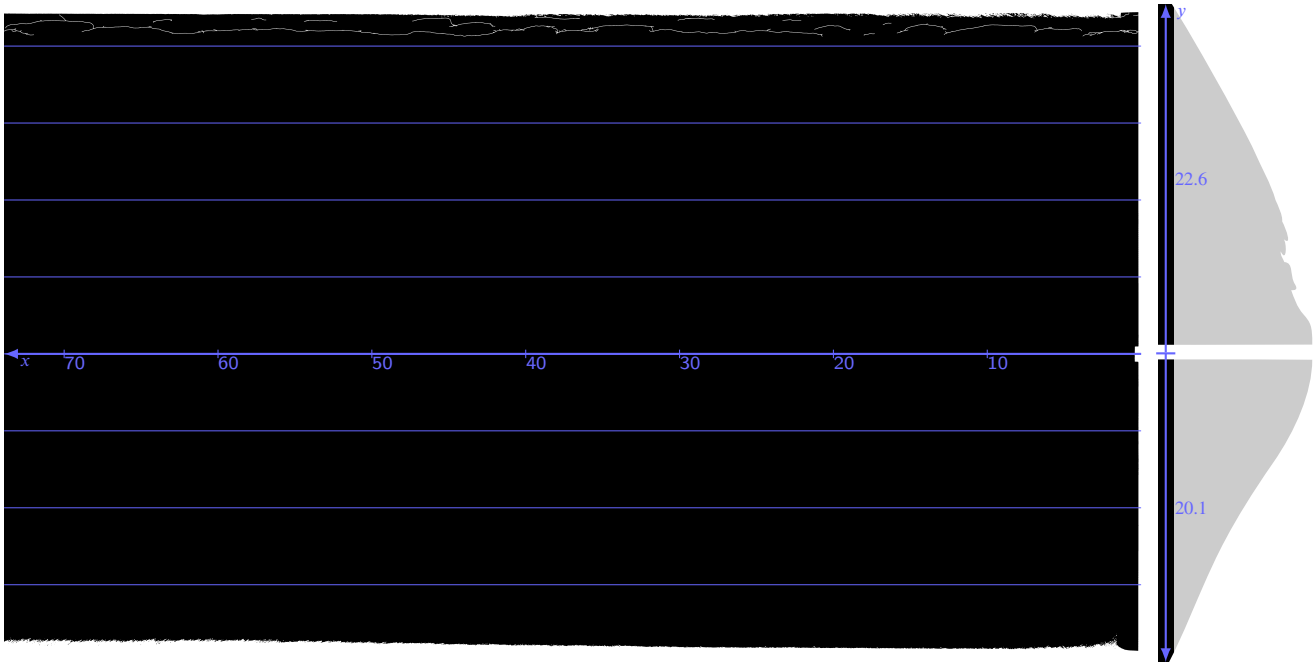

(h) Section microscopy at $z = 9.00\,\text{mm}$.

Figure 8: (continued)

5. Numerical evaluation

5.1. Simulation of rail bending

The proposed method relies on the bending moment in the rail caused by the passing train. This initial study only considers slow-moving trains and, therefore, the analyzes are quasi-static. The parameters for calculating the bending moments are given in Table 1. Additionally, the code is available as supplementary material (see `rail_bending_model.zip`). The vehicle parameters are from the simulated freight train in Nielsen et al.[18]. We simulate a standard 50E3 rail profile as an Euler-Bernoulli beam, supported by sleepers with 0.65 m spacing. An under-rail-pad is also included. Finally, the ballast properties are taken from Li et al.[12], and a representative support width of 0.5 m was chosen for each sleeper. Many of these stiffness parameters do not significantly influence the resulting moment, which is of interest in the present study. The main factors influencing the moment distribution are the wheel spacings and the wheel load.

Figure 1 gives the bending moment for a certain position of the train relative to the sleepers. As the train moves forward, the bending moment under the two camera positions changes slightly. This effect is shown in Figure 9a. At Camera A, the moment is rather constant and very close to zero. However, at Camera B, the moment fluctuates when rolling between two sleepers. To maximize the method's sensitivity for all positions, we must maximize the minimum moment over such a cycle by adjusting the camera position, L_c (see Figure 1 for definition of L_c). Figure 9b shows how the minimum moment varies with camera position. The maximum moment is also included as a reference. The black dot marks the minimum moment at the position of camera B that maximizes the minimum moment. For the parameters in Table 1, this bending moment is 3.8 kNm. The DIC method can calculate the average surface strain and then also the bending moment. Hence, a varying bending moment when rolling does not pose an issue for the proposed method.

Table 1
Simulation parameters, see also Figure 1 for definitions of lengths

Parameter	Value
Elastic modulus of ground	150 MPa
Poissons ratio of ground	0.3
Depth of ground under sleeper	2.0 m
Ground thickness (plane strain)	0.5 m
Sleeper dimension along track	0.25 m
Sleeper spacing	0.65 m
Spring stiffness of rail pad	120 kN/mm
Rail elastic modulus	210 GPa
Rail moment of inertia	2074 cm^4
Total rail length (free ends)	65.0 m
Wheel spacing, L_wh	1.8 m
Bogie spacing, L_b	8.8 m
Wagon spacing, L_wa	13.8 m
Load from each wheel	122.6 kN

Figure 4 shows how the SNR increases with increasing load. Therefore, it would be advantageous to increase the bending moment of 3.8 kNm. With the parameters from Table 1, the maximum and minimum bending moments seen by the rail are 8.0 kNm and −21.1 kNm respectively. To calculate this, 50 different train positions relative the sleepers are considered. By adjusting the wheel positions of the train the bending moment seen by the camera can be increased, without increasing the load on the rail. Using $L_\mathrm{wh} = 1.0$ m, $L_\mathrm{b} = 8.0$ m, and $L_\mathrm{wa} = 14.0$ m, the maximum and minimum rail bending moments become 6.1 kNm and −20.3 kNm respectively. However, the minimum bending moment seen by camera B becomes 5.1 kNm.

There are several recommendations for determining the maximum allowable rail bending stress[21]. Most are based on the rail material's yield strength, σ_y, and give the maximum bending stress, $\sigma_\mathrm{b,max}$, as

$$\sigma_\mathrm{b,max} = \frac{\sigma_\mathrm{y} - \sigma_\mathrm{T}}{(1+A)(1+B)(1+C)(1+D)} \tag{1}$$

where σ_T is the thermal stress. The safety factors A, B, C,

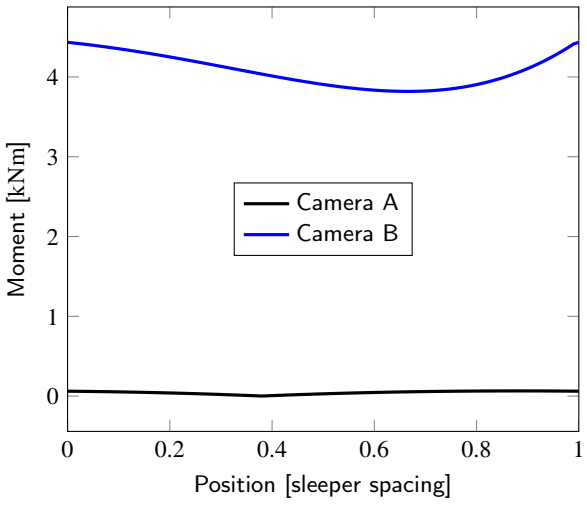

(a) Moment variation over one sleeper spacing for Camera B at position $L_c = 1.15$ m.

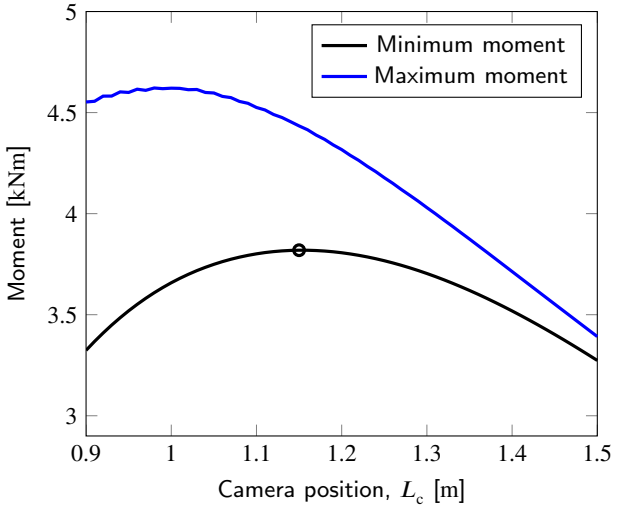

(b) The maximum and minimum moment in rail beneath Camera B depending on its distance, L_c, from the wheel.

Figure 9: Moment variation beneath cameras during rolling. (a) shows the moment variation for the position of Camera B indicated by the black circle in (b).

and D vary. Denoting $s = (1 + A)(1 + B)(1 + C)(1 + D)$, the different recommendations in Robnett et al.[21] yield $s \in [1.81, 2.14]$. Taking the yield stress for R260 of 534 MPa[15] and assuming a 30 °C temperature drop, the conservative maximum bending stress $\sigma_{b,max}$ become 228 MPa. For the rail foot of an 50E3 rail, this corresponds to a bending moment of −49 kNm. Hence, the wheel load can be doubled without violating this limit. In this case, the minimum bending moment seen by camera B become 10.2 kNm, giving a good SNR according to Figure 4.

5.2. Finite element modeling of cracks

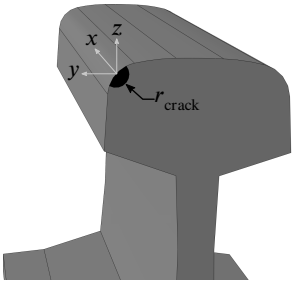

(a) Cracked location in rail

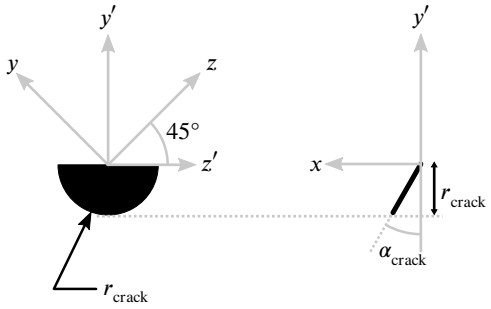

(b) Dimensions of crack

Figure 10: Dimensions of the crack in the finite element model

In Figure 7, the heterogeneity in the surface strain due to cracks was shown. The investigation of the crack network in Figure 8 reveals a maximum crack depth of about 3 mm. However, the crack networks are intricate with many interacting cracks. To better understand what the surface strains can tell about the cracks, a study with a finite element model of a cracked rail is performed in the present section.

To study the sensitivity of the crack detection method to crack inclination, the crack angle, α_{crack}, in Figure 10b, is considered. Note that the coordinate system here is different from the coordinate system used on the field sample. The crack is further parameterized by the crack depth, r_{crack}. This depth is also radius of the crack projection onto the yz-plane. As shown in Figure 10a, the crack is located in the middle of the gauge corner on the nominal rail profile. In the simulations, the rail is subjected to a bending moment of 15 kNm, but as the analysis is linear the results can be scaled to the

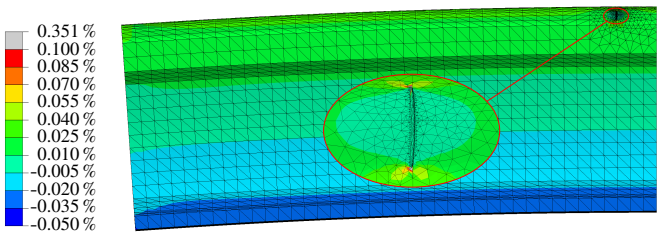

Figure 11: Longitudinal strain for a 5 mm, 45° inclined, crack.

desired bending moment.

Figure 11 shows the normal strain component along the rail for a large, inclined, crack. The displacements are amplified 50 times to show the deformation. We apply the bending moment to the left side and symmetry boundary conditions on the right side. We are thus effectively considering two symmetric cracks. The strain field is homogeneous up to the symmetry boundary and, therefore, this has negligible influence.

As was discussed in conjunction with Figure 2, the DIC method uses a discrete set of points to calculate the strain. With the system used in this study, the facet size was 19 pixels. This size corresponds to approximately 0.25 mm. So to calculate the strain, we created a grid with 0.25 mm spacing onto which the calculated displacements are interpolated. The strain in each segment is then calculated as the numerical derivative using this grid. Hence, the results are affected by grid translations. However, this is the case when using DIC as well.

Figure 12a shows the strain along the x-axis for two crack angles with a crack depth of 2.5 mm. For the more inclined crack, the strain concentration is higher. This finding is confirmed for all studied crack depths, see Figure 12b. More importantly, however, is that the surface strain correlates very well with the crack depth. Although a 45° crack results in larger strains, the influence of angle is much smaller than that of the crack depth.

The DIC results in Figure 7 show a strain of about 0.5% in the identified cracks. Although the strain over cracks are dependent on the discretization, it can be compared with the results in Figure 12 as these have an equivalent discretization. By analyzing the crack networks in Figure 8, a maximum depth of about 3 mm was found. The results in Figure 12 predict a crack depth of approximately 1.5 mm for this case. However, these predictions assume an ideal elliptical crack whose opening is perpendicular to the applied stress. The investigated rail's crack network is complicated with various angles and interactions between cracks and surface irregularities. However, the predicted strain levels are in the same

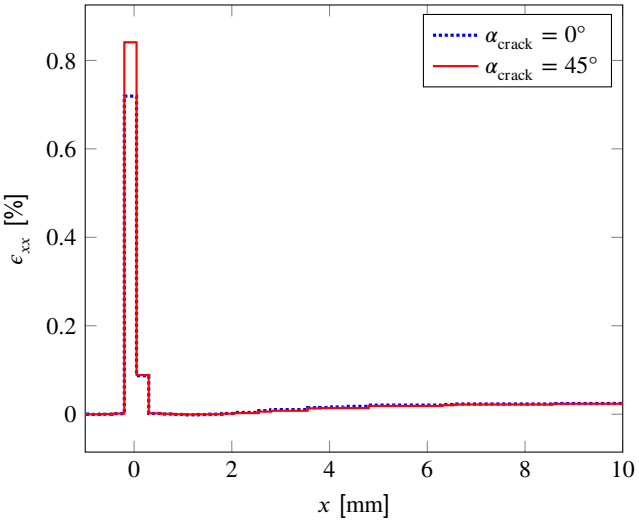

(a) Strain field for $r_{crack} = 2.5$ mm

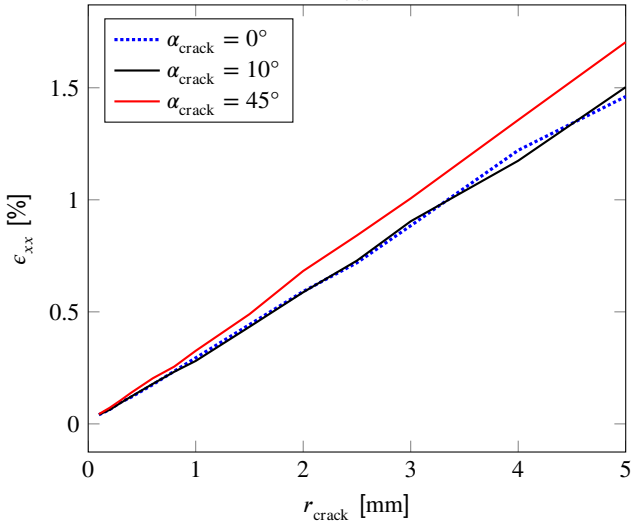

(b) Max strain

Figure 12: FE-modeling results

order of magnitude as the experimental results. These predictions are thus useful to understand how the surface strain field can predict the crack severity. Still, when going from the 3-dimensional crack network and representing that as a 2-dimensional strain field, a certain amount of information will be lost.

6. Discussion

The discussion is split in three parts. First, the main findings in the present study are elaborated. Second, solutions to the challenges remaining before the method can be used in industry are discussed. Finally, possible future enhancements of the method are proposed.

6.1. Main findings

The proposed method utilizes the variation in rail bending stresses inflicted by the measurement train. To assess the feasibility of the proposed method, the bending stresses have been calculated with the finite element method, using Euler-Bernoulli beam elements, supported by sleepers on a flexible ground. Using the more advanced Timoshenko beam theory would affect the displacements but not the bending moment. The local wheel and sleeper contact regions are introduced as point loads. The sleeper width is 0.25 m and the sleeper spacing is 0.65 m. Hence, the contact conditions between the sleeper and the rail may influence the bending stresses. Due to the large variability in these conditions in field, however, it is out of scope for the present study to account for these effects. The goal is to determine the order of magnitude for bending stresses occurring in the rail. Furthermore, the influence of train configurations were briefly discussed in Section5.1. The bending moment under camera B could be increased significantly without increasing the overall rail loading.

The field sample used for crack characterization was taken from a main line in the Swedish railway network, see Meyer et al.[16] for further details. Stock and Pippan[24] produced crack depths around 2 mm in controlled laboratory conditions after 10^5 wheel passages during accelerated testing (23 ton wheel load). For field tests, they found a crack depth of 1.1 mm after 125 MGT in the R260 rail. Their result gave slightly lower crack depths than the 3 mm identified in the present study. But the depth magnitudes are similar and show that the rail sample have representative damage for the present evaluation.

For the freight train parameters in Table 1 and the DIC system used in the present work, the SNR is too low to detect the cracks. However, as previously shown (see Section 5.1), the bending moment can be increased to above 10 kNm by adjusting the wheel positions in the measurement train and increasing the wheel load. This change can be done without exceeding standard rail bending moment limits. Additionally, the available objective lenses for the DIC system had a 40×60 mm field-of-view. Using a higher magnification can further increase the SNR. However, the choice of bending moment and magnification will depend on the type and size of the defect to be detected. From a maintenance planning perspective, it is advantageous with early warnings. But detecting small defects that do not require any action is not necessary.

6.2. Remaining challenges

6.2.1. Reliance on a speckle pattern

A crucial drawback with the DIC method as it has been used in the present study is its reliance on a speckle pattern. The pattern was painted on the rails in two stages, which is not feasible when used for condition monitoring. However, operational rail surfaces have a texture, as can be seen in Figure 13. The commercial DIC system could not identify a pattern based on this texture. Nevertheless, it might still be

possible to identify displacements using specialized image processing, potentially in combination with machine learning. Furthermore, as previously discussed, contaminants on the rail surface may introduce additional structure on the surface. In some materials, such as cast iron, natural speckle patterns has been successfully used[23].

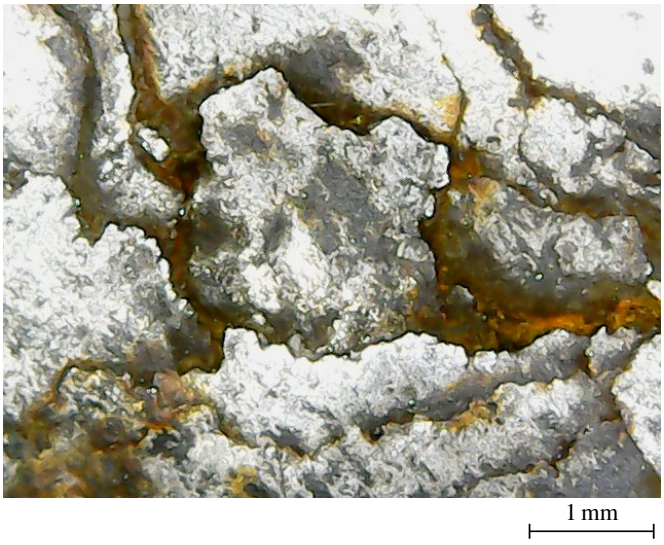

Figure 13: Image of cracked rail surface

Another possible solution is to use a laser speckle pattern, cf. the work by Zheng et al.[26]. Shining monochromatic light on a non-smooth surface produces an interference pattern. This pattern can be used to identify facets and thus to calculate the deformations. However, it is sensitive to the relative positions of the monochromatic light and the image sensor. Furthermore, to the authors' knowledge, stereo DIC has yet to be developed with a laser speckle pattern.

The above solutions, to circumvent the application of paint for generating sufficient contrast, require further research. However, both methods have already been used in the literature. Therefore, it is realistic to assume that methods avoiding painted speckle patterns can be developed.

6.2.2. Interpretation of results

An efficient condition monitoring system depends on interpretable results that eventually lead to decision making. One advantage with the proposed method is that the results are explicit in terms of individual cracks. This feature is in contrast to other NDT methods that consider so-called "indications", cf. A388/A388M-19[2]. The more explicit damage detection by the present method can enable differentiation of defects, such as head checks and squats. In this work, an initial study showed the method's sensitivity to the crack depth. However, more work is required to assess the severity of the damage based on the DIC results. Both numerical studies of different crack morphologies and field studies on various defects should be conducted. Eventually, limit values for various damage types are required for efficient integration in maintenance planning.

6.2.3. Design of measurement system

As the DIC system is sensitive to vibrations, it must be softly suspended to avoid transferring train vibrations. The camera positions must also adapt to the train motion to capture the rail surface. For example, the center part of each wagon (at Camera A) will move laterally during cornering. Furthermore, the camera height must be constant to maintain image focus. While this is a challenging engineering problem, it seems solvable by using established techniques. Even so, these challenges may limit the maximum speed at which the system can operate.

In the present study, the DIC system has a pixel density of about 78 pixels/mm. So if a width of 30 mm is measured, 182 520 pixels/mm are recorded. An 8-bit grayscale then result in 183 kB/mm (8 bits = 1 B). However, a certain overlap between the images will be required to create a continuous measurement. Assuming 200 kB/mm, a train moving at 100 km/h will produce about 5.6 GB/s. This requirement is achievable with consumer-grade electronics, such as a Thunderbolt 3 cable (max speed 5 GB/s), by utilizing parallel data transfer. A high-performance network communication

standard, such as HDR InfiniBand, is commercially available with five times higher transfer rates. Another concern is the data amounts generated. Characterizing a railway line of 500 km would require 100 TB of data, which is also possible with consumer electronics. However, it is not necessary to permanently store the raw data. Once it has been processed, the result can be compressed to a few risk parameters for longer sections of the rail. Even if stereo DIC is used and these figures are doubled, the data handling is straight forward to parallelize. Furthermore, if a doubled magnification is used to improve the sensitivity, the data speed and size requirement is quadrupled. In such a case, the use of e.g. HDR InfiniBand might be beneficial.

6.3. Future developments

The proposed system does not require additional actuators, as in e.g. ultrasonic and eddy-current testing. It is therefore suitable for combination with other measurement techniques. For example, the large defects that ultrasonic testing should detect may be obscured by surface defects. By combining the proposed method with ultrasonic testing, such surface defects may be characterized. Potential risk areas, in which defects may be hidden from the ultrasonic measurements, can then be identified. Furthermore, Rajamäki et al. [20] suggest that eddy-current measurements should be complemented by visual inspection methods. For that purpose, the proposed method could be used as a high-fidelity visual inspection system.

The current study only includes strains due to a positive rail bending moment, compared to a zero moment reference state. This method is the typical application of DIC in crack detection. Most cracks in fatigue loaded samples are perpendicular to the surface and the applied loading direction. Compressive loading will close these cracks. However, typical rail cracks are oriented at an angle when breaking the surface. Therefore, examining the strain field of rails exposed to large negative bending moments could increase the method's detection capabilities. This measurement can be accomplished by using special lenses as illustrated in Figure 14. Additionally, the crack tip displacements during compressive bending stresses can give further information about the crack opening stress. This will be related to the thermal stress in the rail, potentially giving indications of the risks for sun-kinks during summer and rail fracture during winter.

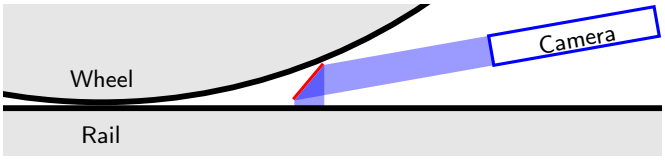

Figure 14: Custom lens (red) to capture the compressive strains close to the wheel

7. Concluding remarks

To improve the knowledge of the current rail health status of a railway network, we have proposed a new method for efficient rail crack monitoring. The load from a measurement train induces a strain field on the rail head surface that is measured using Digital Image Correlation (DIC). For bending moments within the safe limits for rail loading, a sufficient signal-to-noise ratio is achieved allowing cracks to be detected.

As opposed to currently used non-destructive tests, the present method can explicitly describe the surface-breaking cracks. Supplemented by finite element analyses, we have demonstrated that the method is highly sensitive to crack depth. Using serial sectioning, the 3-dimensional crack networks are characterized and the correlation to the surface strain field is shown. With further research, additional crack characteristics may be identified, such as differentiating between squats and head-checks. Finally, possible strategies for industrial implementations are discussed. In conclusion the

proposed method has the potential to improve rail condition monitoring.

8. Acknowledgements

This work is part of the activities within the CHARMEC Centre of Excellence at Chalmers University of Technology. Parts of the study have been funded within the European Union's Horizon 2020 research and innovation programme in the project In2Track2 under grant agreement no. 826255. Our colleague Sebastian Almfeldt at the Architecture and Civil Engineering department kindly lended us their DIC equipment along with his expertise, which was greatly appreciated by the authors.

CRediT authorship contribution statement

Knut Andreas Meyer: Conceptualization, Methodology, Investigation, Writing - Original Draft, Writing - Review & Editing, Visualization. **Daniel Gren:** Investigation, Writing - Review & Editing. **Johan Ahlström:** Resources, Writing - Review & Editing. **Anders Ekberg:** Resources, Writing - Review & Editing.

References

[1] Abidin, I.Z., Tian, G.Y., Wilson, J., Yang, S., Almond, D., 2010. Quantitative evaluation of angular defects by pulsed eddy current thermography. NDT and E International 43, 537–546.

[2] ASTM International, 2019. A388/A388M Standard Practice for Ultrasonic Examination of Steel Forgings. doi:https://doi.org/10.1520/A0388_A0388M-19.

[3] Cannon, D.F., Edel, K.O., Grassie, S.L., Sawley, K., 2003. Rail defects: An overview. Fatigue and Fracture of Engineering Materials and Structures 26, 865–886.

[4] Deutschl, E., Gasser, C., Niel, A., Werschonig, J., 2004. Defect detection on rail surfaces by a vision based system, in: IEEE Intelligent Vehicles Symposium, 2004, IEEE. pp. 507–511.

[5] Gao, Y., Tian, G.Y., Li, K., Ji, J., Wang, P., Wang, H., 2015. Multiple cracks detection and visualization using magnetic flux leakage and eddy current pulsed thermography. Sensors and Actuators A: Physical 234, 269–281.

[6] Greene, R.J., Yates, J.R., Patterson, E.A., 2007. Crack detection in rail using infrared methods. Optical Engineering 46, 051013.

[7] Heiming, M., Candfield, J., Lochman, L., 2012. Track Maintenance & Renewal. URL: http://www.cer.be/sites/default/files/publication/2353_7473-11_MARKET_STRATEGY_A4_FINAL.pdf.

[8] Innotrack, 2008. D4.4.1 – Rail inspection technologies. Technical Report. Innotrack.

[9] Jessop, C., Ahlström, J., Persson, C., Zhang, Y., 2020. Damage evolution around white etching layer during uniaxial loading. Fatigue and Fracture of Engineering Materials and Structures 43, 201–208.

[10] Kishore, M., Park, J., Song, S., Kim, H., Kwon, S.G., 2019. Characterization of defects on rail surface using eddy current technique. Journal of Mechanical Science and Technology 33, 4209–4215.

[11] Lee, J.S., Hwang, S.H., Choi, I.Y., Choi, Y., 2020. Estimation of crack width based on shape-sensitive kernels and semantic segmentation. Structural Control and Health Monitoring 27, 1–21.

[12] Li, X., Nielsen, J.C., Torstensson, P.T., 2019. Simulation of wheel–rail impact load and sleeper–ballast contact pressure in railway crossings using a Green's function approach. Journal of Sound and Vibration 463, 1–16.

[13] Lidén, T., Joborn, M., 2016. Dimensioning windows for railway infrastructure maintenance: Cost efficiency versus traffic impact. Journal of Rail Transport Planning & Management 6, 32–47.

[14] Marais, J.J., Mistry, K.C., 2003. Rail integrity management by means of ultrasonic testing. Fatigue and Fracture of Engineering Materials and Structures 26, 931–938.

[15] Meyer, K.A., Ekh, M., Ahlström, J., 2018a. Modeling of kinematic hardening at large biaxial deformations in pearlitic rail steel. International Journal of Solids and Structures 130-131, 122–132.

[16] Meyer, K.A., Nikas, D., Ahlström, J., 2018b. Microstructure and mechanical properties of the running band in a pearlitic rail steel: Comparison between biaxially deformed steel and field samples. Wear 396-397, 12–21.

[17] Mohan, A., Poobal, S., 2018. Crack detection using image processing: A critical review and analysis. Alexandria Engineering Journal 57, 787–798.

[18] Nielsen, J.C.O., Kabo, E., Ekberg, A., 2009. Alarm limits for wheel–rail impact loads – part 1: rail bending moments generated

by wheel flats. Technical Report. Chalmers University of Technology. Gothenburg. URL: https://research.chalmers.se/en/publication/107339.

[19] Pohl, R., Erhard, A., Montag, H.J., Thomas, H.M., Wüstenberg, H., 2004. Ndt techniques for railroad wheel and gauge corner inspection. NDT and E International 37, 89–94.

[20] Rajamäki, J., Vippola, M., Nurmikolu, A., Viitala, T., 2018. Limitations of eddy current inspection in railway rail evaluation. Proceedings of the Institution of Mechanical Engineers, Part F: Journal of Rail and Rapid Transit 232, 121–129.

[21] Robnett, Q.L., Thompson, M.R., Hay, W.W., Tarabji, S.D., Peterson, H.C., Knutson, R.M., Baugher, R.W., 1975. Technical data bases report, Ballast and foundation materials research program, Report no. FRA-OR&D-76-138. Technical Report. U.S. Department of Transportation. Washington, D.C. URL: https://railroads.dot.gov/sites/fra.dot.gov/files/fra_net/15881/1975_TECHNICAL%20DATA%20BASES%20REPORT%20BALLAST%20AND%20FOUNDATION.PDF.

[22] Rowshandel, H., Nicholson, G.L., Davis, C.L., Roberts, C., 2011. A robotic approach for NDT of RCF cracks in rails using an ACFM sensor. Insight: Non-Destructive Testing and Condition Monitoring 53, 368–376.

[23] Sjögren, T., Persson, P.E., Vomacka, P., 2011. Analysing the Deformation Behaviour of Compacted Graphite Cast Irons Using Digital Image Correlation Techniques, in: Science and Processing of Cast Iron IX, Trans Tech Publications Ltd. pp. 470–475. doi:10.4028/www.scientific.net/KEM.457.470.

[24] Stock, R., Pippan, R., 2014. Rail grade dependent damage behaviour - Characteristics and damage formation hypothesis. Wear 314, 44–50.

[25] Vijaykumar, V.R., Sangamithirai, S., 2015. Rail defect detection using Gabor filters with texture analysis. 2015 3rd International Conference on Signal Processing, Communication and Networking, ICSCN 2015 , 6–11.

[26] Zheng, Q., Mashiwa, N., Furushima, T., 2020. Evaluation of large plastic deformation for metals by a non-contacting technique using digital image correlation with laser speckles. Materials and Design 191, 108626.

[27] Zhuang, L., Wang, L., Zhang, Z., Tsui, K.L., 2018. Automated vision inspection of rail surface cracks: A double-layer data-driven framework. Transportation Research Part C: Emerging Technologies 92, 258–277.